IOPscience iopscience.iop.org

Home Search Collections Journals About Contact us My IOPscience

Two-dimensional systems with competing interactions: microphase formation versus liquid–vapour phase separation

This article has been downloaded from IOPscience. Please scroll down to see the full text article.

2010 J. Phys.: Condens. Matter 22 415103

(http://iopscience.iop.org/0953-8984/22/41/415103)

View the table of contents for this issue, or go to the journal homepage for more

Download details:
IP Address: 128.131.48.66
The article was downloaded on 15/09/2010 at 16:42

Please note that terms and conditions apply.

J. Phys.: Condens. Matter **22** (2010) 415103 (10pp) doi:10.1088/0953-8984/22/41/415103

Two-dimensional systems with competing interactions: microphase formation versus liquid–vapour phase separation

Dieter F Schwanzer and Gerhard Kahl

Institut für Theoretische Physik and Center for Material Science (CMS), Technische Universität Wien, Wiedner Hauptstraße 8-10, A-1040 Wien, Austria

E-mail: schwanzer@cmt.tuwien.ac.at

Received 5 July 2010
Published 13 September 2010
Online at stacks.iop.org/JPhysCM/22/415103

Abstract

Based on extensive integral-equation calculations and on complementary Monte Carlo simulations we have investigated the phase behaviour of a class of two-dimensional model systems where particles interact via short-range attractive and long-range repulsive potentials. While for a particular member of this class of systems microphase formation has already been studied in detail in the literature, we have provided evidence that—depending on the model parameters that define this class of systems—both microphase formation and liquid–vapour transitions can be observed. For those systems that form microphases we have focused on the homogeneous fluid which is encountered at higher temperatures. By analysing the structure functions we show that already in this disordered phase a precursor of the low-temperature microphases can be identified: the wavenumber k_c, which specifies those density fluctuations against which the system becomes unstable when forming microphases at lower temperatures also plays an important role in the homogeneous phase. For those systems that show liquid–vapour phase separation we find clear trends in the position of the critical point and in the location of the coexistence branches.

(Some figures in this article are in colour only in the electronic version)

1. Introduction

Over the past few years, a remarkable number of theoretical contributions have been dedicated to elucidating the spontaneous formation of pattern (or microphase formation), induced by competing interparticle interactions operating on different length scales [1–11]. In these potentials an attractive component, dominant at short distances, is in concurrence with a repulsive contribution which dominates at larger distances. In two dimensions, the observed patterns are clusters, stripes and bubbles (or inverse clusters). Similar morphologies are also observed in three-dimensional systems: spherical clusters, ordered arrangements of cylinders, or layers (lamellae). The emergence of these patterns is the more astonishing as the underlying interactions are spherically symmetric. In nature, certain colloidal systems are characterized by such potentials, where typically the attraction originates from the depletion forces while the repulsion stems from the (weakly) screened charge of the colloids. Experimental evidence for spontaneous pattern formation in such systems has been given both in two [12–16] and three [17–20] dimensions.

A profound insight into the properties of microphase separating systems was provided in previous work of Imperio, Reatto and co-workers, who focused mainly on two-dimensional systems [1, 2, 4, 5, 7]. Their investigations are based on a model that was first proposed in [22] where particles interact via a potential $\Phi(r)$, given by

$$\Phi(r) = \begin{cases} \infty & r \leqslant \sigma \\ -\epsilon_a \dfrac{\sigma^2}{R_a^2} \exp\left(-\dfrac{r}{R_a}\right) + \epsilon_r \dfrac{\sigma^2}{R_r^2} \exp\left(-\dfrac{r}{R_r}\right) & r > \sigma \end{cases} \quad (1)$$

where σ is the hard-core (HC) diameter, and ϵ_a (ϵ_r) and R_a (R_r) represent the strength and the range of the attractive (repulsive) contribution to the potential tail in $\Phi(r)$ beyond σ, respectively. Most of the above investigations were based on

 © 2010 IOP Publishing Ltd Printed in the UK & the USA

the following set of potential parameters: $\epsilon_a = \epsilon_r$, $R_a = \sigma$ and $R_r = 2\sigma$. The list of the sometimes quite surprising phenomena that were studied by Imperio, Reatto and co-workers for this system is quite exhaustive: it comprises spontaneous and induced pattern formation [1], the transition from the microphase formation to the homogeneous liquid [2], the influence of confinement on the pattern formation [4], and the rheological properties [5]. Very recently, an order parameter theory was put forward to investigate the details of the phase diagram of the three-dimensional counterpart [10].

To be more specific, Imperio, Reatto and co-workers found out that, with increasing temperature, the transition from the mesophase formation regime to the homogeneous fluid is accompanied by a peak in the specific heat, which arises as the mesophases break up. Detailed investigations of the specific heat in this process provide evidence that most likely the system undergoes neither a first-nor a second-order transition, but rather (or possibly) a Kosterlitz–Thouless transition [2]. Furthermore, the transformation from the cluster to the stripe phase, which is induced by an increasing density, is presumed to be of first order. Of particular relevance for our work is also a density functional (DFT) approach proposed by Archer [6], which leads to a phase diagram that is in qualitative (but not quantitative) agreement with the simulation data obtained in [2]. In particular in this contribution a closed expression for a wavenumber k_c was put forward, which specifies those density fluctuations against which the system becomes unstable, thus leading to the respective microphase formation.

The aim of the present contribution is to study phase transition scenarios for systems with short-range attractive and long-range repulsive potentials from a more general point of view. This includes not only the phenomenon of microphase formation but also the conventional liquid–vapour transition. To this end we have considered the potential $\Phi(r)$, defined in equation (1), as the basis of a class of systems by introducing two parameters, E and R: the first one is the ratio between the interaction strengths, $E = \epsilon_r/\epsilon_a$, the latter one the ratio of the range, $R = R_r/R_a$, of the two contributions to the tail of $\Phi(r)$ beyond σ. From our investigations of a large portion of the (E, R) plane we are able to identify those regions where the systems show either of the two phase behaviour scenarios. For microphase forming systems we find evidence that precursors of the emerging microphases can already be identified in the structure functions of the homogeneous phase that the system forms at higher temperatures. Further, we show that the aforementioned wavenumber k_c plays a key role in the structural properties of microphase forming systems: for *all* systems characterized by the same k_c value, the static structure factors, $S(k)$, show a maximum at $k = k_c$. On the other hand, we show that systems with competing interactions are able to display a conventional liquid–vapour transition which only occurs as the repulsive tail is sufficiently weak and/or sufficiently short-ranged. For those systems we have traced out the phase diagrams and we discuss trends in the localization of the coexistence branches and of the (extrapolated) critical points as the system parameters vary.

Our investigations are mainly based on integral-equation approaches (whenever convergence could be achieved): the Ornstein–Zernike (OZ) equation is complemented by the Percus–Yevick (PY) and the hypernetted chain (HNC) closure relations [23]. These data are complemented for selected systems and particular state points by Monte Carlo simulations.

This paper is organized as follows: in the subsequent section we briefly present the model and the theoretical tools we have used, namely integral-equation approaches and Monte Carlo simulations; technical and numerical details have been transferred to the appendix. In section 3 we discuss the results obtained for the two phase transition scenarios and the paper is closed with concluding remarks.

2. Model and theoretical approaches

2.1. Model

In our system particles interact via the spherically symmetric potential $\Phi(r)$ introduced in equation (1). Further, the system is characterized by its temperature T (with $\beta = (k_B T)^{-1}$) and an area density ρ. Throughout we will use reduced units, i.e. $\rho^\star = \rho\sigma^2$, $r^\star = r/\sigma$ and $k^\star = k\sigma$; for the temperature T we have used the arbitrary temperature scale introduced in [1], namely that for $R = 2$ and $E = 1$, $\beta U(\sigma) = -1$. For simplicity henceforth the asterisk is omitted.

With the parameters E and R introduced above we create a class of potentials. In our investigations we have varied E and R over the ranges [0, 1] and [0.5, 2.5], respectively. In an effort to demonstrate the role of E and R on the shape of the potential, we show in figure 1 the ensuing potentials as we vary the two parameters independently, while keeping the other one fixed. We observe that both range and strength of the attractive and of the repulsive components of the potentials are influenced in a highly sensitive way by these parameters. A more detailed and quantitative discussion of these trends will be given in section 3.1.

2.2. Integral-equation approach

To obtain information about the structural and thermodynamic properties of the system we use on the one side integral-equation approaches. They are based on the OZ equation [23]:

$$h(r) = c(r) + \rho \int \mathrm{d}\vec{r}'\, h(|\vec{r} - \vec{r}'|)c(r'), \tag{2}$$

where $c(r)$ and $h(r)$ are the direct and total correlation functions, respectively; the radial distribution function, $g(r)$, is given by $g(r) = h(r) + 1$. Furthermore, we introduce the indirect correlation function, $\gamma(r) = h(r) - c(r)$. The OZ equation is complemented by a closure relation, establishing a functional relation between $h(r)$, $c(r)$ and $\Phi(r)$. In this paper we have used the PY closure:

$$g(r) = \exp[-\beta\Phi(r)][h(r) - c(r) + 1] \tag{3}$$

and the HNC relation:

$$g(r) = \exp[-\beta\Phi(r) + h(r) - c(r)]. \tag{4}$$

The numerical solution of the OZ equation in combination with one of the closure relations is for two-dimensional systems a

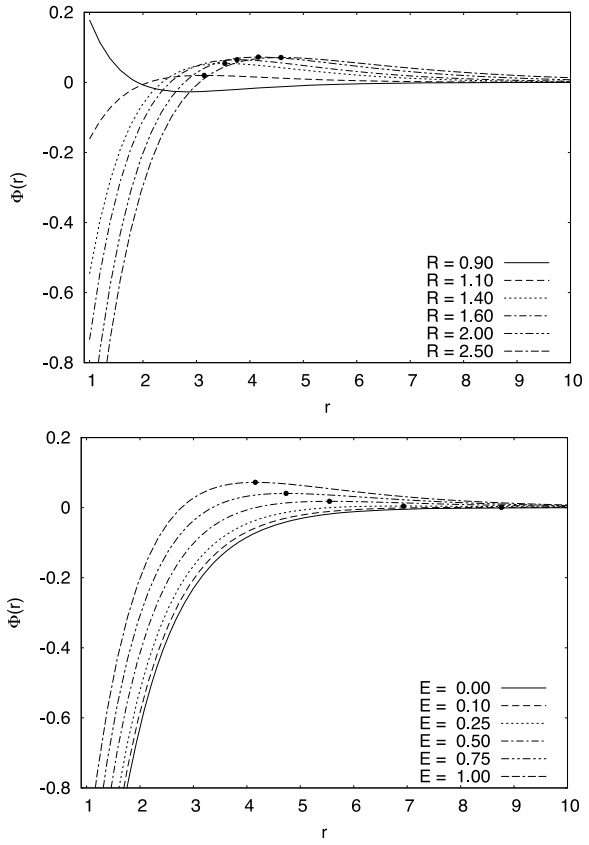

Figure 1. Interparticle potentials $\Phi(r)$ (cf equation (1)) of the class of systems investigated in this contribution for different E and R values; only the σ range outside the hard-core is shown. Top panel: $E = 1.0$ and selected R values as indicated in the inset; bottom panel: $R = 2.0$ and selected E values as indicated in the inset. The full dots mark the maximum in $\Phi(r)$.

considerably more delicate task than for a three-dimensional system; details on this technical issue are summarized in the appendix.

Once the correlation functions have been determined, we can calculate the thermodynamic problems via standard relations [23], suitably adapted for the two-dimensional case. The pressure P evaluated via the virial route is given by

$$\frac{\beta}{\rho}P = 1 - \frac{\pi}{2}\rho\int_0^\infty \mathrm{d}r\,\beta\frac{\mathrm{d}\Phi(r)}{\mathrm{d}r}r^2 g(r)$$
$$= 1 - \frac{\pi}{2}\rho\int_\sigma^\infty \mathrm{d}r\,\beta\frac{\mathrm{d}\Phi(r)}{\mathrm{d}r}r^2 g(r) + \frac{\pi}{2}\rho\sigma^2 g(\sigma^+) \qquad (5)$$

where the last term in the second line of the above relation takes into account the hard-core contribution to the interaction $\Phi(r)$. Within the HNC framework [23], a closed *exact* expression is available for the excess (over ideal gas) chemical potential, μ^{ex}, namely

$$\beta\mu^{\mathrm{ex}}_{\mathrm{HNC}} = \rho\int \mathrm{d}\vec{r}\,[\gamma(r) - h(r) + \tfrac{1}{2}h(r)\gamma(r)]. \qquad (6)$$

For the PY closure relations, a closed, *approximate* expression has been derived by Lee for $\mu^{\mathrm{ex}}_{\mathrm{HNC}}$ [24], which provides reasonably accurate results for quite a few simple fluids. Within this framework, the excess chemical potential is given by

$$\beta\mu^{\mathrm{ex}}_{\mathrm{PY}} = \rho\int \mathrm{d}\vec{r}\,\ln[1+\gamma(r)] + \left[\frac{\gamma(r) - h(r)}{\gamma(r)}\right]. \qquad (7)$$

The coexistence branches in the phase diagram are obtained by equating, at a given temperature, the pressure and the chemical potential of the coexisting phases (for numerical details see, for instance, [25]).

2.3. Monte Carlo simulations

In an effort to complement the integral-equation-based results we have performed extensive Monte Carlo (MC) simulations in the canonical ensemble. These simulations have been carried out with N particles in a square box of side length L, featuring periodic boundary conditions. We have used between 400 and 4000 particles in our simulation runs. A considerable speed-up of the simulation was achieved by performing simulations on a discrete spatial grid, a method that has been introduced by Panagiotopoulos [26]. To be more specific, we have sub-divided the simulation box into 4096 × 4096 equally sized squares, which define thus the available, discrete particle positions. A further increase in the numerical efficiency of the simulations was achieved by using the cell-list method [27]. Simulations extended over 2000 000–4000 000 MC sweeps, where a sweep corresponds to N attempted particle moves. Correlation functions were obtained as averages over at least 80 000 independent particle configurations.

From the positions of the particles we have evaluated static and thermodynamic properties: the static structure factor, $S(k)$, has been evaluated directly from the positions of the particles $\mathbf{r}_i$ $(i = 1, \ldots, N)$ via

$$S(k) = \frac{1}{N}\langle\rho_{\mathbf{k}}\rho_{-\mathbf{k}}\rangle \qquad (8)$$

with $\rho_{\mathbf{k}} = \sum_j \exp[\mathrm{i}\mathbf{k}\mathbf{r}_j]$.

For the evaluation of the pressure we have used expression (5). While the integral in this relation was computed by averaging the virial over a sufficiently large number of configurations, $g(\sigma^+)$ was computed by a careful extrapolation of $g(r)$ for $r \to \sigma^+$. For the evaluation of the excess chemical potential we have used the Widom insertion method [27].

3. Results

3.1. Overview

In figure 2 we provide an overview over the investigated systems, where the symbols mark those systems that have been investigated both by integral-equation approaches as well as MC simulations. By varying the parameters E and R introduced above within the ranges [0, 1] and [0.5, 2.5], respectively, we cover a large variety of interparticle potentials.

The systems can be classified as follows:

- for systems that are located in the dark-shaded (red) area, microphase formation occurs: at intermediate and high temperatures the system forms a homogeneous

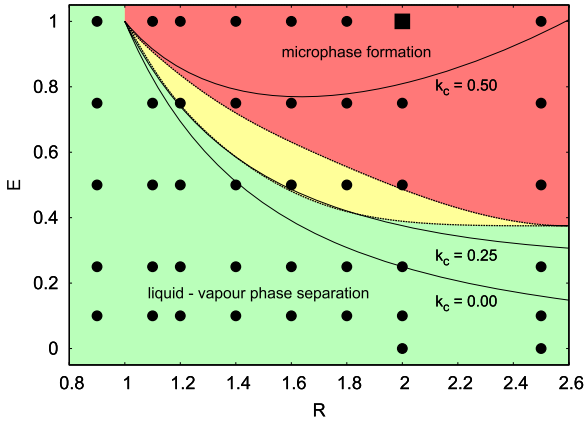

Figure 2. Overview over the investigated systems (● or ■) specified by parameter values E and R (cf text); the square indicates the choice of parameters used by Imperio and Reatto [1, 2, 4, 5]. For systems located in the medium-shaded (green) area, a liquid–vapour phase separation is observed, while systems in the dark-shaded (red) area show microphase formation. For systems located in the narrow, light-shaded (yellow) region, no conclusive answer for either of the two scenarios could be given. Furthermore, the figure contains lines along which the wavenumber k_c is constant with values as indicated (see text and equation (9)).

fluid phase, while below a density-dependent temperature microphase formation is observed. An estimate for this transition line for a parameter combination $E = 1$ and $R = 2$ has been given by Imperio and Reatto [2] (see the discussion below);

- for states located in the green area, a liquid–vapour phase separation scenario was found: for these states we could identify a coexistence line well above the no-solution line of the integral-equation approaches;
- finally, we are left with a few systems located between the medium-shaded (green) and the dark-shaded (red) area, populating the narrow, light-shaded (yellow) region: here, neither integral-equation approaches nor simulations could provide sufficient evidence for either of the two scenarios.

At this point, a few remarks on the influence of the potential parameters E and R on the phase separation scenario are in order. In figure 3 we show in two panels the explored region in (E, R) space: the top panel provides information about the position $r_{\max}$ of the maximum in the long-range tail of $\Phi(r)$, while the bottom panel gives information about the values of the potential at this maximum. From these figures we learn that microphase formation occurs only if the position of the maximum in $\Phi(r)$, $r_{\max}$, is less than ∼5.5; in addition, the repulsive shoulder must be sufficiently strong, i.e. $\Phi(r_{\max}) \gtrsim 0.02$. Consequently, if, on the other hand, the repulsive tail is sufficiently long-ranged and not too strong, then the systems displays a conventional liquid–vapour phase transition. The trends in $\Phi(r)$, as we vary the parameters E and R, independently, are displayed in figure 1: keeping E fixed, and increasing R shifts $r_{\max}$ to larger r values and $\Phi(r_{\max})$ increases monotonically, but obviously reaches saturation in the observed R range. On the other hand, keeping R fixed and increasing E shifts $r_{\max}$ to smaller r values; now $\Phi(r_{\max})$ is

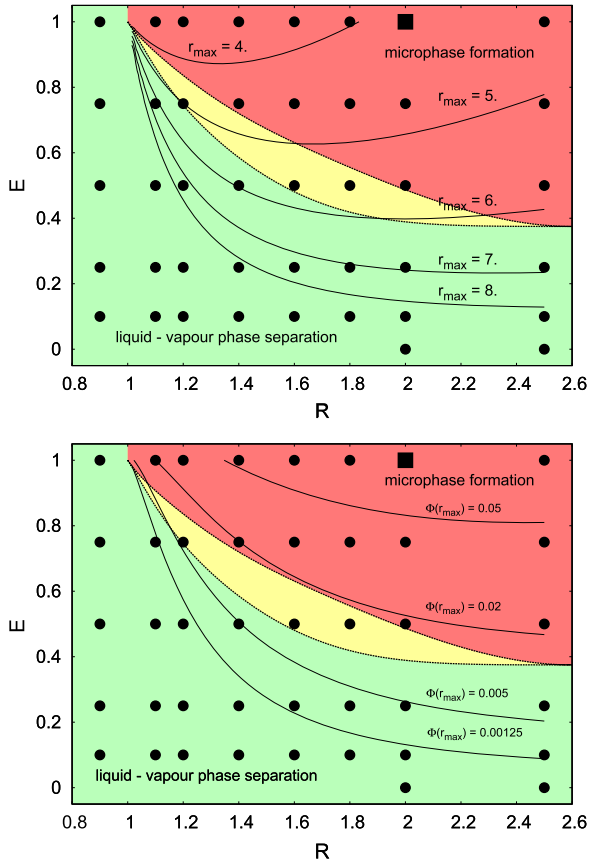

Figure 3. Overview over the investigated systems (● or ■) specified by parameter values E and R. Top panel: lines specify systems for which the position of the long-range repulsion, $r_{\max}$, is constant with a value as indicated. Bottom panel: lines specify systems for which the maximum in the long-range repulsion, $\Phi(r_{\max})$, attains a constant value as indicated.

monotonically increasing. For a related discussion of this issue in three-dimensional systems we refer to [21].

3.2. Systems with microphase formation

For systems that populate the dark-shaded (red) area of figure 2 microphase formation occurs below a certain, density-dependent temperature. Above this temperature the system forms a homogeneous fluid phase.

In a DFT approach for microphase forming systems with competing interactions, Archer [6] was able to derive a closed expression for k_c, which represents the wavelength against which the system becomes unstable, forming thereby microphases. The explicit expression for k_c is given by

$$k_c = \sqrt{\frac{\Gamma - 1}{R_r^2 - \Gamma R_a^2}} = \frac{1}{R_a}\sqrt{\frac{\Gamma - 1}{R^2 - \Gamma}}$$
$$\text{with } \Gamma = \left(\frac{\epsilon_r R_r^2}{\epsilon_a R_a^2}\right)^{5/2} = (E R^2)^{5/2}; \tag{9}$$

obviously k_c depends only on the potential parameters and not on the state parameters. In figure 2 we have included lines along which k_c is constant. Of course, for $k_c = 0$ we expect a conventional liquid–vapour transition and thus the $(k_c = 0)$ line should coincide with the limits of the green

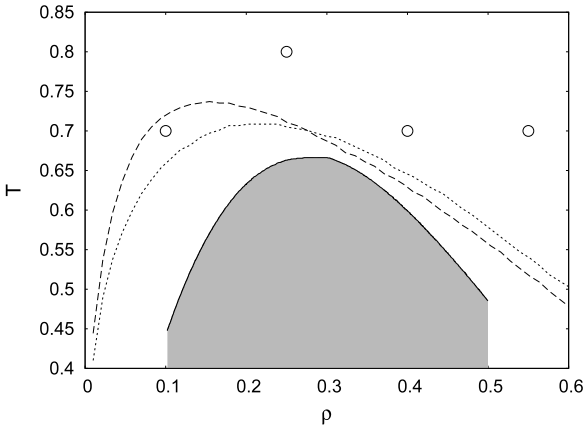

Figure 4. Investigated state points (○) of a system characterized by $E = 1$ and $R = 2$. The dashed and the dotted lines represent the no-solution lines of the HNC and the PY integral-equation approach, respectively. The full line delimits the region in phase space below which the system shows microphase formation (estimate taken from [1]).

area. The obvious discrepancy between these two lines reflects the limitation of the DFT concept; on the other hand, we will soon provide evidence that the actual value of k_c, evaluated via relation (9), fits remarkably well in the overall picture of microphase forming systems.

We start our discussion with the 'standard' microphase forming system investigated in detail by Imperio and Reatto [1, 2, 4, 5] and specified by $E = 1$ and $R = 2$, focusing on a few selected state points. Since essentially all aspects related to microphase formation of this particular system have been addressed in previous work (cited above), we focus here on the disordered phase which is encountered for all densities and at sufficiently high temperatures. In figure 4 we present an estimate for the region where—according to the results presented in [1]—the system shows microphase formation. In addition, we have plotted the so-called no-solution lines evaluated via the PY and HNC approximations, i.e. the line below which the numerical solution of the respective integral-equation approach breaks down. The discrepancy between the boundary of microphase formation and the no-solution lines provides evidence of the limitations of integral-equation approaches. In our discussion we focus on four state points, indicated in figure 4. They are chosen in close vicinity to the no-solution line of the integral-equation approaches.

For these four state points, the radial distribution functions, $g(r)$, and the static structure factors, $S(k)$, are displayed in figures 5 and 6. For all states we observe a surprisingly good agreement between the data obtained from the simulations and the integral-equation approaches. For these four state points we have verified from 'visual inspection' of the simulation data that microphase formation has not set in, yet. Even more surprising is the fact that PY and HNC provide data that are essentially identical. This is a rather unconventional observation, since for most (simple) liquids PY and HNC show distinct differences for the structure functions [23]. The radial distribution functions display in particular for small and intermediate densities a rather unconventional behaviour: a small side peak close to the pronounced main peak is followed at intermediate and large distances by extremely long-range oscillations. Only for the highest densities we recover the 'usual' oscillatory behaviour around unity, expected for a radial distribution function. These features, in combination with the pronounced main peak in $g(r)$, can be interpreted as precursors of the microphases that the system is expected to form at lower temperatures. Also the structure factors, shown in figure 6, display a rather unconventional behaviour: for all state points investigated we observe extremely long-range oscillations in

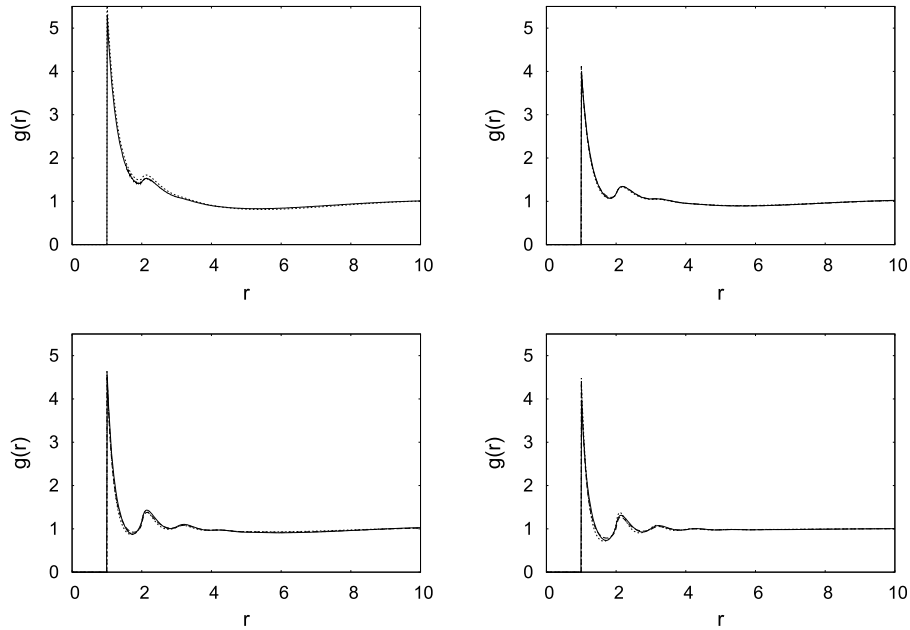

Figure 5. Radial distribution functions, $g(r)$, of the systems defined by $E = 1$ and $R = 2$ and by the state points specified in figure 4 by the symbols; the (T, ρ) values are given by: top line—(0.7, 0.1), (0.25, 0.8), bottom line—(0.7, 0.4), (0.7, 0.55). Symbols: full line—MC simulation data, dotted line—PY results, dashed–dotted line—HNC results.

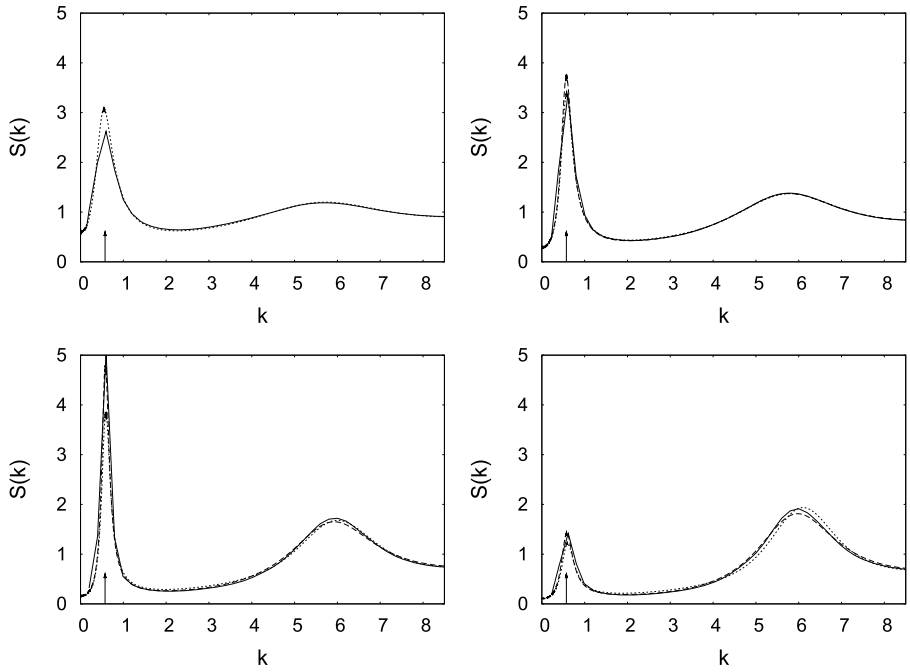

Figure 6. Static structure factors, $S(k)$, of the systems defined by $E = 1$ and $R = 2$ and by the state points specified in figure 4 by the symbols; the (T, ρ) values are given by: top line—(0.7, 0.1), (0.25, 0.8), bottom line—(0.7, 0.4), (0.7, 0.55). Symbols: full line—MC simulation data, dotted line—PY results, dashed–dotted line—HNC results. The vertical arrows indicate the value of k_c for this particular system.

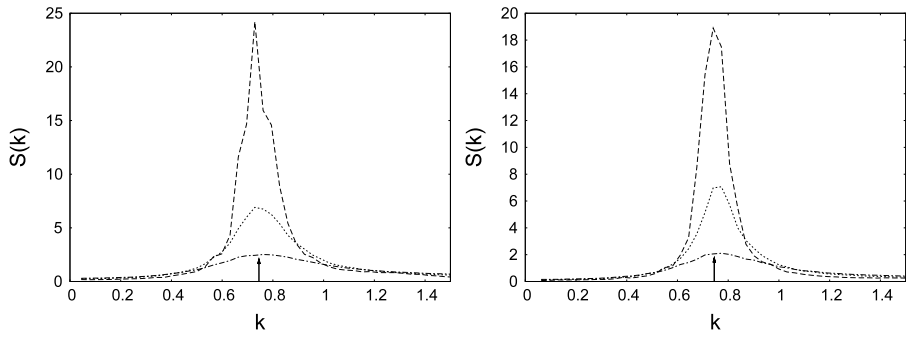

Figure 7. Static structure factors, $S(k)$, of a system specified by $E = 1$ and $R = 1.2$. Densities: $\rho = 0.2$ (left panel) and $\rho = 0.4$ (right panel). Temperatures: $T = 0.10$ (dashed line), $T = 0.15$ (dotted line) and $T = 0.20$ (dashed–dotted line). The vertical arrow indicates the value of k_c for this particular system.

k. The height of the main peak in $S(k)$ shows a strongly non-monotonic behaviour as the density increases, attaining sometimes remarkably high values; note that, at the highest density investigated, the second peak is even higher than the first peak. In addition we have indicated by a vertical arrow the value of k_c that characterizes the system—cf equation (9). Although k_c was originally derived for the *ordered* microphases encountered at lower temperatures, its value agrees even for the *disordered*, homogeneous phase remarkably well with the position of the main peak of $S(k)$ for all systems investigated. Again, this observation can be interpreted as a precursor of the microphases expected to occur at lower temperatures.

The relevance of k_c for microphase forming systems and its state *independence*—cf equation (9)—are visualized in figures 7 and 8 via simulation data. In figure 7 we display the static structure factor $S(k)$, evaluated via (8), of a microphase-forming system. We have fixed two values for the density (i.e. $\rho = 0.2$ and 0.4) and vary T; the chosen temperature values are sufficiently low so that the system spontaneously forms patterns. We observe that—while the height of the main peak in $S(k)$ strongly changes with temperature—its position remains essentially fixed at the value of the wavenumber k_c. Alternatively we keep in figure 8 the temperature fixed (at sufficiently low values) and vary the density: the chosen ρ values correspond to the formation of clusters ($\rho = 0.2$), lamellae ($\rho = 0.4$) and bubbles ($\rho = 0.6$). Again, the position of the main peak in $S(k)$ does not vary with increasing density and perfectly coincides with k_c. We point out that remarkable differences in the peak heights of the inverted microphase (i.e. bubbles) with respect to the clusters and lamellae can be observed.

To highlight the central role of k_c for the structural properties of microphase-forming systems even more, we

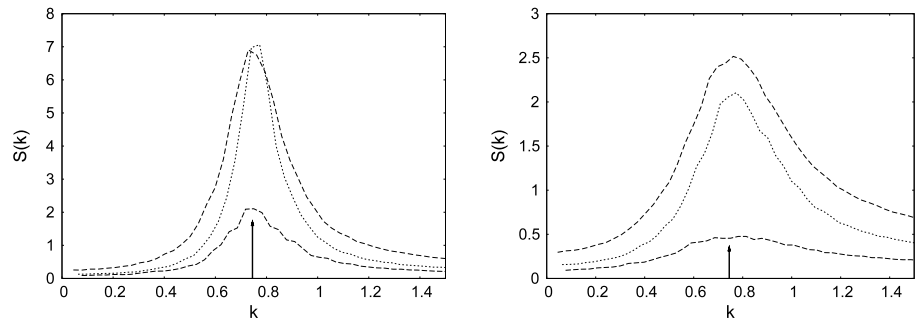

Figure 8. Static structure factors, $S(k)$, of a system specified by $E = 1$ and $R = 1.2$. Temperatures: $T = 0.15$ (left panel) and $T = 0.2$ (right panel). Densities: $\rho = 0.2$ (dashed line), $\rho = 0.4$ (dotted line) and $\rho = 0.6$ (dashed–dotted line). The vertical arrow indicates the value of k_c for this particular system.

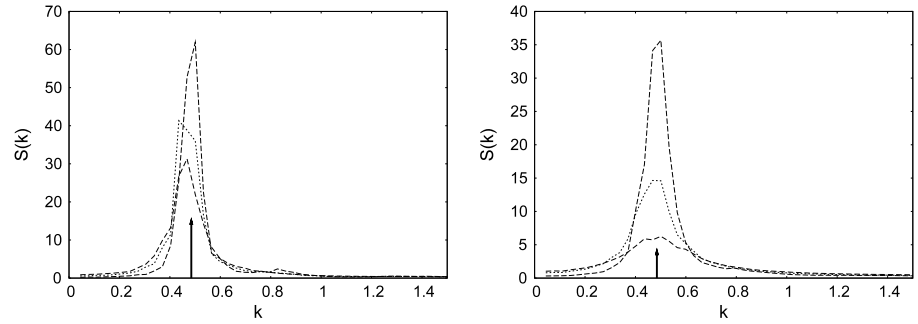

Figure 9. Structure factors, $S(k)$, of systems A, B and C (as defined in the text), at $T = 0.50$ and $\rho = 0.20$ (left panel) and $T = 0.7$ and $\rho = 0.2$ (right panel). The vertical arrow indicates the value of k_c for this particular system. Symbols: dashed line—system A, dotted line—system B, and dashed–dotted line—system C.

finally chose our potential parameters in such a way as to yield a particular value of k_c. We define systems A, B and C, characterized by the following parameter pairs (E, R): system A—$(0.750, 1.60)$, system B—$(0.750, 1.80)$ and system C—$(0.905, 2.50)$; these parameters lead for all systems to essentially the same value of k_c, namely $k_c \approx 0.485$. In figure 9 we present results for the static structure factors of the three systems for two different temperatures and densities. Again, we see that the height of the main peak in $S(k)$ varies strongly with temperature and density as well as with the values of E and R; however, its position is essentially unchanged at $k = k_c$.

3.3. Systems with liquid–vapour phase separation

Systems that populate the medium-shaded (green) area depicted in figure 2 show a conventional liquid–vapour phase separation. For this class of systems we start our discussion with an overview over the phase diagrams: in each of the panels depicted in figure 10 we have kept the value of E fixed, varying R systematically over a representative range. The coexistence lines have been determined by equating, at fixed temperature, the pressure and the chemical potential of the coexisting phases. Thermodynamic properties were calculated via the PY integral-equation approach.

In an effort to discuss the ensuing trends of the localization of the coexistence lines in the (T, ρ) diagram on a more quantitative level, we have *estimated* the critical point (in terms of a critical temperature and a critical density), by assuming the usual power law for the density difference between the coexisting phases as a function of temperature. As E increases from 0 to 1, we observe that the critical temperature decreases and that the coexistence lines flatten. Keeping E fixed and increasing R, both the critical temperature as well as the critical density decrease monotonically. As the value of R approaches the boundaries of the medium-shaded (green) area depicted in figure 2, ρ_c tends to zero; thus the liquid–vapour phase transition converts into microphase formation.

We conclude our discussion of the liquid–vapour phase separating systems with the presentation of a few structure functions, choosing a representative system ($E = 0.50$ and $R = 1.40$) for which we display the structure functions in figure 11. The state points are located both on the vapour and on the liquid side close to the phase boundaries. Even in the very dilute vapour phase, $g(r)$ shows a rather pronounced main peak, which is reproduced in excellent agreement between the simulation and the integral-equation data. On the liquid side of the phase diagrams, $g(r)$ shows again a pronounced main peak and an asymmetric side peak. In contrast to the microphase-forming systems (cf figure 5) we observe a worse agreement between the simulation data and the integral-equation results.

4. Conclusions

We have investigated the two scenarios of phase behaviour that emerge for a class of two-dimensional systems with competing

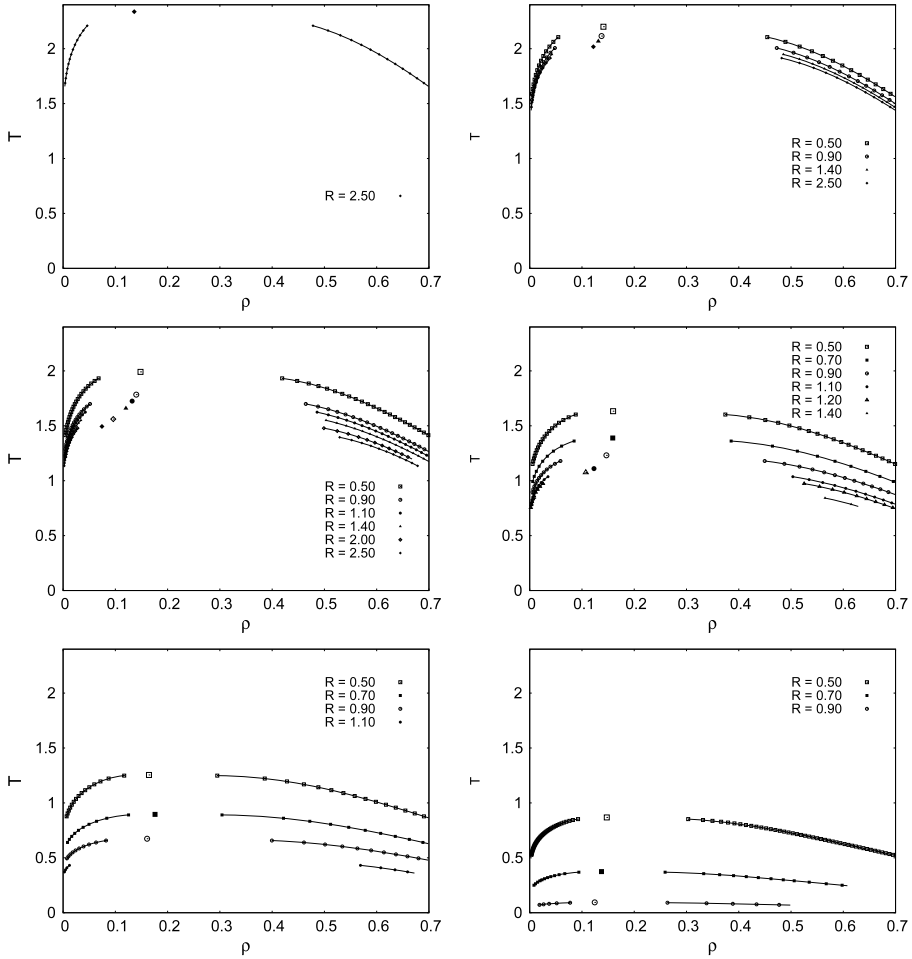

Figure 10. Liquid–vapour coexistence lines in the (T, ρ) plane for selected systems investigated in this contribution. In each panel we keep E fixed, varying R over a representative range (as indicated). Critical points, represented by isolated symbols, are estimated via a power law.

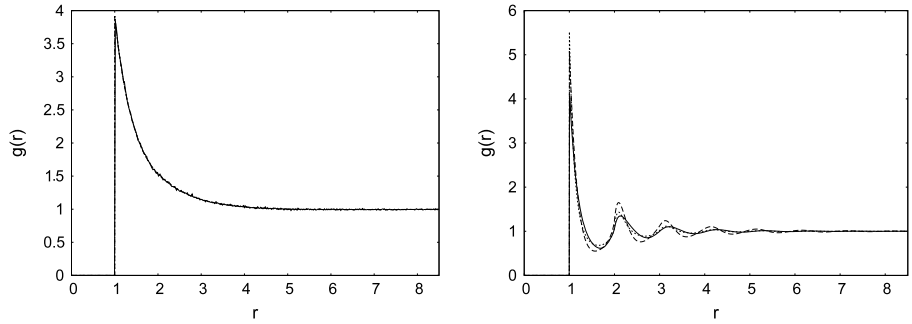

Figure 11. Radial distribution function, $g(r)$, of a liquid–vapour phase-separating system ($E = 9.50$ and $R = 1.4$) for a vapour ($T = 0.85$ and $\rho = 0.0095$) and a liquid state ($T = 0.85$ and $\rho = 0.70$). Symbols: full line—MC simulation data, dashed line—PY results, dotted line—HNC results.

interactions, operating on different length scales, namely microphase formation and liquid–vapour phase separation. In our model the two contributions to the interactions are parametrized via two exponential tails of opposite sign and different decay lengths. Investigations have been carried out with integral-equation approaches (using the PY and the HNC closure relations) and with Monte Carlo simulations. By systematically varying the potential parameters we could identify those regions in parameter space where the systems show either microphase formation or a conventional liquid–vapour phase transition.

For the microphase-forming systems we have focused in particular on the homogeneous fluid phase which occurs at sufficiently high temperatures and at any densities. For the structure functions we have found an astonishingly good agreement between the simulation data and integral-equation results. Even more surprisingly, the data obtained via the two closure relations essentially coincide. This observation

is very surprising since for simple liquids different closures lead in general to distinctively different results for the structure functions. Although the chosen temperatures are sufficiently high, we can identify in the structure functions even in the homogeneous fluid phase precursors of those microphases that the system will form at lower temperatures: in particular, the main peak of the structure factor is located at the wavenumber k_c, which specifies those density fluctuations against which the system becomes unstable. Results of MC simulations confirm that the peak position in $S(k)$ is located at k_c and that it does not change neither with density nor with temperature, as predicted by DFT.

For the liquid–vapour phase-separating systems we have traced out the coexistence lines and have provided estimates for the location of the critical point. A systematic variation of the potential parameters gives evidence of clear trends in the location of the phase boundaries. Agreement of the structural data between integral-equation data and computer simulation results is good, but of less quality than the one observed in the microphase-forming systems.

Acknowledgments

Financial support by the Austrian Research Fund (FWF) under project nos. P19890-N16 and W004 is gratefully acknowledged.

Appendix

The OZ equation (2) was solved in combination with a closure relation, using a standard Picard algorithm. In this iterative scheme, Fourier transforms from r to k space, and vice versa, are frequently used. In contrast to the three-dimensional case, numerical Fourier transforms in two-dimensional space cannot take direct advantage of fast Fourier transform (FFT) techniques and routines.

According to the formalism presented in detail in [28–30], a function $f(r)$ and its two-dimensional Fourier transform, $\tilde{f}(k)$, are related via the following expressions [31]:

$$\tilde{f}(k) = 2\pi \int_0^\infty \mathrm{d}r\, r f(r) J_0(kr)$$
$$f(r) = \frac{1}{2\pi} \int_0^\infty \mathrm{d}k\, k \tilde{f}(k) J_0(kr), \tag{10}$$

where $J_0(kr)$ is the zeroth-order Bessel function. Following steps that are explained in detail in [30], the integrals in equation (10) can be transformed into a convolution-type integral which, after being transformed into k space, decouples into a product of two integrals. While one of these integrals can be calculated analytically, the other one can be evaluated efficiently using an FFT routine. In these manipulations a substitution of variables takes place, substituting r by R and k by K via the following relations:

$$r = \exp(R) \qquad k = \exp(K). \tag{11}$$

The grid in R and K space is equally spaced, with ΔR and ΔK satisfying the usual relation, $\Delta R \Delta K = \pi/2^M$, imposed by the FFT formalism, where M is a suitably chosen integer. As a consequence of relations (11), the grid in r and k space is no longer equally spaced. Furthermore, a lower bound for the R grid, $R_m = \ln r_m$, has to be chosen.

In the following, we provide information on how the actual values of ΔR, M and R_m influence the structural and thermodynamic properties of the system. For all our investigations a value of $R_m = -7$ (corresponding to $r_m \sim 0.0009\sigma$) has turned out to be suitable. In figure A.1 we display the radial distribution function, $g(r)$, of one of the systems investigated and the spacing in r space, Δr, for different choices of ΔR and M. Throughout, we have used in our investigations $\Delta R = 0.002$ and $M = 13$. This choice represents a reasonable compromise between computational costs and sufficient accuracy to grasp the full details of the long-range behaviour of the radial distribution functions, guaranteeing thereby a reliable evaluation of the thermodynamic properties via the expressions presented in section 2.2.

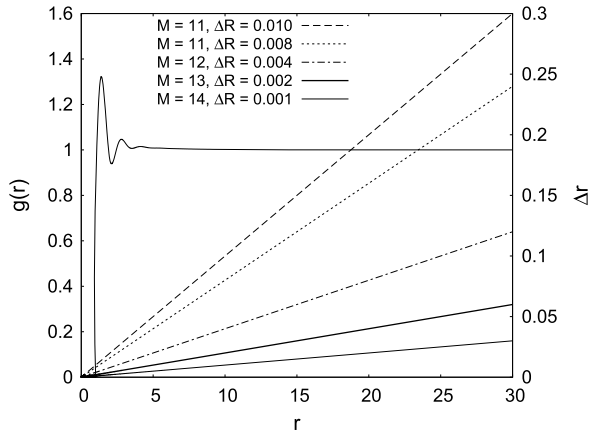

Figure A.1. Left-hand side: radial distribution function, $g(r)$, of a typical system investigated in this contribution as a function of r. Right-hand side: Δr as a function of r, as used in the two-dimensional Fourier transform for various values of M and ΔR (for details, cf appendix).

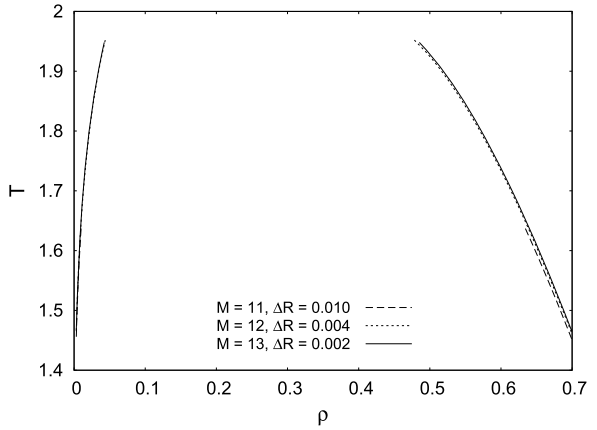

Figure A.2. Liquid–vapour coexistence branches in the (T, ρ) plane of a representative system investigated in this study ($E = 0.10$ and $R = 1.40$), evaluated for different choices of M and R; for details, cf appendix. Note that for $M = 11$ the numerical algorithm breaks down at substantially lower temperatures than for $M = 12$ and 13.

Of course, the actual values of ΔR and M also have influence on the location of the branches of the coexistence lines. In figure A.2 we show the influence of ΔR and M on the coexistence curve for a typical liquid–vapour phase-separating system.

References

[1] Imperio A and Reatto L 2004 *J. Phys.: Condens. Matter* **16** S3769
[2] Imperio A and Reatto L 2006 *J. Chem. Phys.* **124** 164712
[3] Pini D, Parola A and Reatto L 2006 *J. Phys.: Condens. Matter* **18** S2305
[4] Imperio A and Reatto L 2007 *Phys. Rev.* E **76** 040402
[5] Imperio A, Reatto L and Zapperi S 2008 *Phys. Rev.* E **78** 021402
[6] Archer A J 2008 *Phys. Rev.* E **78** 031402
[7] Imperio A, Pini D and Reatto R 2007 *Proc. Workshop 'Collective Phenomena in Macroscopic Systems'* ed G Bertin, R Pozzoli, M Rome and K R Sreenivasan (Singapore: World Scientific)
[8] Archer A J and Wilding N B 2007 *Phys. Rev.* E **76** 031501
[9] Archer A J, Pini D, Evans R and Reatto L 2007 *J. Chem. Phys.* **126** 014104
[10] Archer A J, Ionescu C, Pini D and Reatto L 2008 *J. Phys.: Condens. Matter* **20** 415106
[11] Lee L L, Hara M C, Simon S J, Ramos F S, Winkle A J and Bomont J M 2010 *J. Chem. Phys.* **132** 074505
[12] Klokkenburg M, Dullens R P A, Kegel W K, Erné B H and Philipse A P 2006 *Phys. Rev. Lett.* **96** 037203
[13] Heath J R, Gelbart W M, Sear R P and Chaney S 1999 *Faraday Discuss.* **112** 299
[14] Elias F, Flament C, Bacri J C and Neveu S 1997 *J. Physique* I **7** 711
[15] Ghezzi F and Earnshaw J C 1997 *J. Phys.: Condens. Matter* **9** L517
[16] Seul M and Andelman D 1995 *Science* **267** 476
[17] Bordi F, Cametti C and Sennato S 2007 *Interfaces Against Pollution 2006—Proc. 4th Int. Conf. (Granada, June 2006)*; *Colloids Surf.* A **306** 102
[18] Lu P J, Conrad J C, Wyss H M, Schofield A B and Weitz D A 2006 *Phys. Rev. Lett.* **96** 028306
[19] Stradner A, Sedgwick H, Cardinaux F, Poon W C K, Egelhaaf S U and Schurtenberger P 2004 *Nature* **432** 492
[20] Islam M F, Lin K H, Lacoste D, Lubensky T C and Yodh A G 2003 *Phys. Rev.* E **67** 021402
[21] Pini D, Jialin G, Parola A and Reatto L 2000 *Chem. Phys. Lett.* **327** 209
[22] Sear R P, Chung S W, Markovich G, Gelbart W M and Heath J R 1999 *Phys. Rev.* E **59** R6255
[23] Hansen J P and McDonald I R 2006 *Theory of Simple Liquids* 3rd edn (London: Academic)
[24] Lee L L 1992 *J. Chem. Phys.* **97** 8606
[25] Giacometti A, Pastore G and Lado F 2009 *Mol. Phys.* **107** 555
[26] Panagiotopoulosi A Z 2000 *J. Chem. Phys.* **112** 7132
[27] Frenkel D and Smit B 2002 *Understanding Molecular Simulation* 2nd edn (London: Academic)
[28] Talman J D 1978 *J. Comput. Phys.* **29** 35
[29] Weis J J, Caillol J M and Levesque D 1981 *Mol. Phys.* **44** 733
[30] Hoffmann N, Likos C N and Löwen H 2006 *J. Phys.: Condens. Matter* **18** 10193
[31] Lado F 1971 *J. Comput. Phys.* **8** 417